INSTITUTE OF PHYSICS PUBLISHING JOURNAL OF PHYSICS: CONDENSED MATTER

J. Phys.: Condens. Matter **15** (2003) S2647–S2663 PII: S0953-8984(03)65826-1

Infrared spectroscopic study of the morphology of 3,4,9,10-perylene tetracarboxylic dianhydride films grown on H-passivated Si(111)

Reinhard Scholz[1], **Marion Friedrich**[1], **Georgeta Salvan**[1], **Thorsten U Kampen**[1], **Dietrich R T Zahn**[1] **and Thomas Frauenheim**[2]

[1] Institut für Physik, Technische Universität Chemnitz, D-09107 Chemnitz, Germany
[2] Department Physik, Universität Paderborn, Warburger Strasse 100, D-33098 Paderborn, Germany

Received 8 July 2003
Published 12 September 2003
Online at stacks.iop.org/JPhysCM/15/S2647

Abstract

Infrared spectroscopy is applied to the characterization of 3,4,9,10-perylene tetracarboxylic dianhydride (PTCDA) films grown with organic molecular beam deposition (OMBD) on hydrogen-passivated Si(111). Comparing these films with powder spectra, the films show a preferential orientation of the PTCDA molecules close to coplanar with the substrate surface. For deposition of PTCDA films using laser ablation at 1064 nm, the average orientation of the molecules is more random than in the OMBD-grown films, but we still find some degree of preferential order of the molecules with respect to the substrate surface. The experimental findings are compared to density functional calculations of the single molecule and the two crystalline phases.

1. Introduction

In recent years rapid progress in the technology of organic semiconductors has resulted in new electronic and optoelectronic device applications, including organic light-emitting diodes and organic field-effect transistors [1, 2]. The organic materials exhibit excellent optical and electronic properties, comparable to those of conventional inorganic semiconductors [3–5]. Our research interest focuses on the growth and characterization of organic molecular layers, e.g. of 3,4,9,10-perylene tetracarboxylic dianhydride (PTCDA), on inorganic semiconducting substrates like GaAs and Si. Particular emphasis lies in the interaction of PTCDA molecules with the substrate surface and its influence on the layer growth mode. While other techniques such as scanning tunnelling microscopy (STM) [6] and electron spectroscopies [7] have already been employed for this purpose, infrared spectroscopic investigations targeted at this task are rather rare [8, 9].

In the present work we demonstrate that IR spectroscopy gives some insight into the influence of the growth conditions of PTCDA films on the average orientation of the crystallites. From the experimental results, we derive a model for the dielectric function of the dipolar

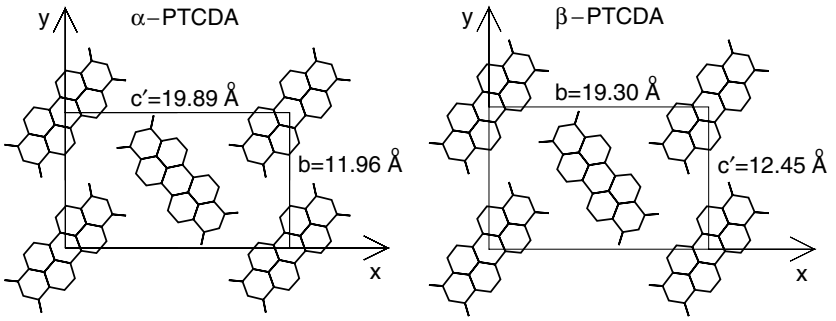

Figure 1. Unit cells of the two monoclinic crystalline phases of PTCDA. Left: α phase, with lattice unit vectors $a = 3.72$ Å, $b = 11.96$ Å and $c = 17.34$ Å [1]. Right: β phase, with lattice unit vectors $a = 3.78$ Å, $b = 19.30$ Å and $c = 10.77$ Å [1]. In both cases, the directions c' visualized are linear combinations of $\boldsymbol{c}$ and $2\boldsymbol{a}$.

internal vibrations of the molecule, and the mode frequencies obtained are compared in detail with density functional calculations of the vibrational modes of the PTCDA molecule and of the two monoclinic crystal phases.

An isolated PTCDA molecule has the point group D_{2h} [10], resulting in 46 infrared active modes of B_u symmetry, including 18 B_{1u} (long axis, x) and 18 B_{2u} (short axis, y) vibrations in the molecular plane and 10 B_{3u} (out of plane, z) modes. As shown in figure 1, the molecules can crystallize in two different monoclinic phases with the crystal space group $P2_1/c$ (C^5_{2h}), called α-PTCDA and β-PTCDA, with different unit cell parameters [1]. In both phases, the two basis molecules in the unit cell are nearly coplanar, defining therefore a preferential growth mode for non-reactive substrates where the first monolayer adsorbs in a geometry close to one of the two bulk phases. For more reactive substrates, a large variety of monolayer geometries have been observed, including one [11] or two [12] basis molecules in the unit cell of the first monolayer, whereas the subsequent layers grow in a geometry close to the one of the bulk phases.

Using IR spectroscopy, the detection of in-plane and out-of-plane vibrational modes depends on the orientation of the molecules relative to the electric field of the infrared light. Consequently, the presence and intensities of the related features in the infrared spectra can be employed to determine the orientation of the molecular planes relative to the substrate surface.

In section 2, we briefly review the sample preparation and experimental set-up before discussing the resulting infrared spectra in section 3. Section 4 is devoted to a detailed data analysis based on a model dielectric function which is subsequently used in section 5 for a determination of the preferential orientation of the molecules in the different samples. In section 6, we assign the most prominent IR-active modes by comparing the experimental mode frequencies with a density functional tight-binding calculation of the vibrational modes of an isolated PTCDA molecule. Furthermore, we compare the calculated mode splittings for the two crystalline phases with the observed spectra. The paper is concluded in section 7.

2. Experimental details

As a substrate, we used p-type (111)-oriented Si wafers with a doping level of $(1.5–3.5) \times 10^{15}$ cm^{-3}. These wafers were cleaned and hydrogen passivated by etching in HF(40%) for 2 min. After the etching procedure, the substrates were immediately transferred into an ultra-high vacuum (UHV) chamber. The surface quality was checked by low-energy

electron diffraction (LEED) and Auger spectroscopy. A sharp 1×1 LEED pattern indicating a good hydrogen passivation of silicon surfaces was obtained, and from peak intensities in the Auger spectra, a carbon contamination of less than 0.1 monolayer was determined. The intensity of the oxygen peaks was much lower than the intensity of the carbon peaks.

On this substrate, PTCDA films were prepared by organic molecular beam deposition (OMBD) evaporating the source material from a Knudsen cell under UHV conditions (base pressure 2×10^{-8} Pa) or by laser ablation (LA) of PTCDA at a wavelength of 1064 nm under high vacuum. The PTCDA source material was pre-purified by thermal gradient sublimation at 400 °C in high vacuum.

During the OMBD growth process, the Knudsen cell temperature as measured by a Pt–PtRh thermocouple was kept at a fixed value in the range of 250–285 °C. The resulting deposition rates onto substrates kept at room temperature were measured by a quartz microbalance and confirmed by post-growth atomic force microscopy measurements to be between 0.15 and 0.28 nm min^{-1}, i.e. below one monolayer (0.3 nm) per minute. These rather low temperatures of the source material and the substrate avoid polymerization into poly-*peri*-naphthalene occurring at higher temperatures [13, 14]. Furthermore, the dependence of the refractive indices of the resulting organic film on the growth temperature indicates that substrates held at room temperature lead to the densest films [8]. It was shown previously using STM that PTCDA films grown on H-passivated Si consist of ordered domains of about 200 Å size [15], and the film growth can be characterized using total current spectroscopy [16] and resonant Raman spectroscopy [17].

For the films grown by LA of the source material, a wavelength of 1064 nm was used in order to avoid destruction or polymerization occurring under LA with higher photon energies in resonance with electronic transitions [18, 19]. High-intensity short laser pulses of 100 ps duration at a repetition rate of 4 Hz were focused to intensities of 4 J cm^{-2}/pulse on the source material, resulting in a growth rate exceeding 100 nm min^{-1}. The deposited film of about 1.3 μm thickness shows a granular structure with lateral crystallite sizes of up to 2 μm. Due to the very high deposition rate and the high thermal energy of the molecules arriving on the substrate held at room temperature, the orientation of the adsorbed molecules in the preferred flat adsorption geometry is partly inhibited by the direct concurrence with the fast growth of crystalline islands. As a consequence, the orientation of the crystallites is less regular than in the film grown by OMBD, but instead they are much larger. In sections 3 and 4, it will be shown in detail how the average orientation of the molecules in the films grown by OMBD and by LA techniques compares, confirming the above growth scenario.

From x-ray diffraction techniques, we have determined a predominance of α-PTCDA in the films grown with OMBD and LA techniques, whereas the PTCDA powder used for reference measurements consists mainly of the β phase.

3. Measured infrared spectra

The infrared spectra were taken *ex situ* using a Bruker IFS 66 FTIR spectrometer. Transmission measurements and angle-dependent reflection measurements in polarized light were carried out with a spectral resolution of 2 or 4 cm^{-1}. For the IR measurements of very thin layers on silicon, 4 cm^{-1} was the best possible resolution for minimal broadening of the infrared features at maximal suppression of substrate interference fringes.

3.1. PTCDA film grown by OMBD

The IR transmission of PTCDA films grown on Si by OMBD was measured at normal incidence, and the absorption coefficient α reported in figure 2 was calculated from the transmission ratio

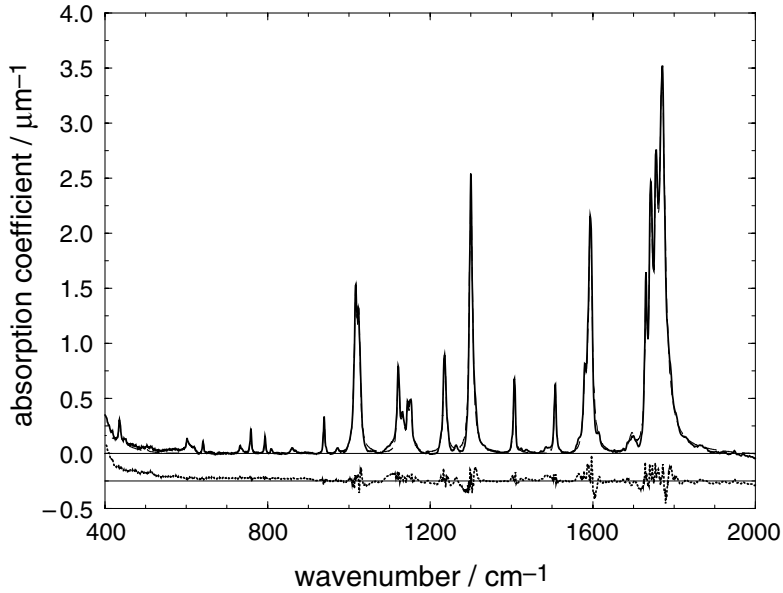

Figure 2. Absorption coefficient of a 220 ± 10 nm PTCDA film grown by OMBD on a H-passivated Si(111) substrate. Thick solid curve: experimental spectra; dashed curve: superimposed fit, compare table 1 and section 4. Dotted line: fit residuum, shifted for clarity to a reference of $-0.25\ \mu m^{-1}$. At low wavenumbers, the experimental data are influenced by the tail of a broad structure below 400 cm^{-1}. In order to make this contribution more evident, it is not removed from the fit residuum.

of the PTCDA-covered Si substrate T_{PTCDA} and of an uncovered reference sample T_{Si}. For the determination of the PTCDA film thickness we used ellipsometry in the visible [20], giving a result of 220 ± 10 nm. The calculated curve superimposed on the measured spectra is based on the dielectric function discussed in section 4.

3.2. Powder spectra

PTCDA powder as obtained from the Lancaster Company was deposited on a gold mirror, and the reflectivity spectra obtained at near normal incidence are displayed in figure 3 [21]. The spectra clearly reveal a peak asymmetry, resulting from a combination of absorptive and dispersive Lorentz profiles, as discussed in more detail in section 4. Compared with the absorption of the OMBD film in figure 2, the most pronounced differences in the peak intensities concern the out-of-plane modes below 900 cm^{-1} and the splittings and intensities of the C=O stretching modes above 1700 cm^{-1}. Details of the superimposed fit of the spectra in figure 3 are discussed in section 4.

3.3. Film deposited with laser ablation

For the sample grown by LA, the IR absorption spectra shown in figure 4 were obtained again from the logarithm of the transmission at normal incidence. As the LA-deposited films exhibit a very rough morphology with crystallites as large as 2 μm, an effective thickness of about 1.1 μm was estimated from a comparison of the absorption related to the in-plane modes with the spectrum of the OMBD film shown in figure 2, corresponding to a thickness of about 1.3 μm

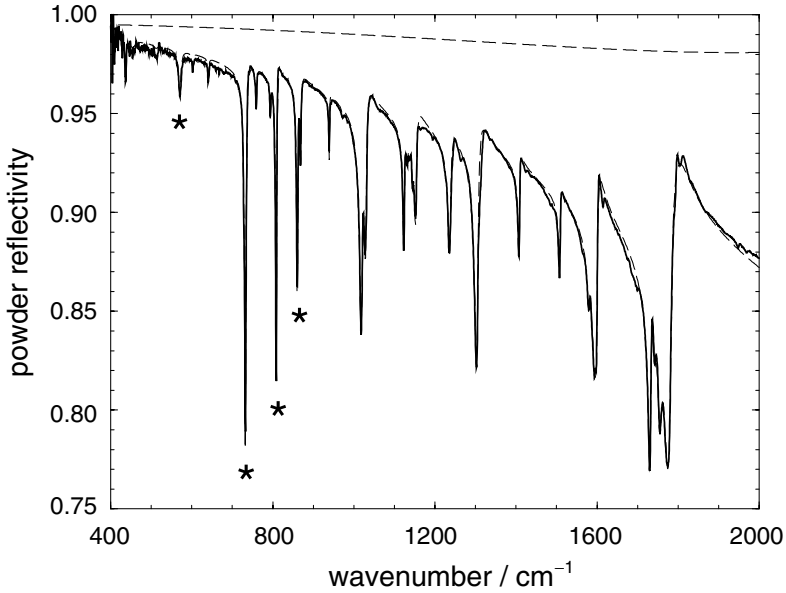

Figure 3. Reflectivity of randomly oriented PTCDA powder on a gold mirror. Thick solid curve: experimental spectra; dashed curves: superimposed fit (upper: background $R_0(\omega)$), compare table 1 and section 4. Out-of-plane modes are marked with $*$.

after corrections for the different average orientations of the molecules (see the next sections for details). The increased contributions of the out-of-plane modes below 900 cm^{-1} indicate a more random orientation of the molecular planes with respect to the substrate surface.

First of all, our results confirm that PTCDA was deposited, since the spectrum in figure 4 is in good agreement with the infrared absorption of PTCDA prepared in a KBr pellet and given in the catalogue (Chemical Abstracts Service Substance Database reg. no 128-69-8), and furthermore, the peak positions agree quite well with the dominating features in the transmission of the OMBD film in figure 2. A possible polymerization occurring for higher growth temperatures or LA at higher photon energy would easily be identified from pronounced differences both in the infrared and Raman spectra [13, 14, 18]. As for PTCDA prepared in KBr pellets, the LA preparation process leads to a loss of the preferential orientation of the molecules with respect to the substrate surface. Even though the out-of-plane features are well visible in figure 4, the orientation of the molecules cannot be considered completely random, as discussed in the data analysis in more detail in section 4.

3.4. Reflectivity of OMBD film

The absorption coefficient of the film deposited with OMBD in figure 2 shows all in-plane features with a size comparable to that of the LA film in figure 4, while the relative size of the out-of-plane features is drastically decreased compared to both the powder in figure 3 and the LA-deposited sample in figure 4. The low absorbance of the out-of-plane features supports an arrangement of the molecular planes nearly parallel to the substrate surface in OMBD films.

In order to further confirm this assumption, additional reflectivity measurements at various angles of incidence were performed, and the results for p-polarized light are displayed in figure 5. While spectra recorded using s-polarized light (not shown) exhibit only strong

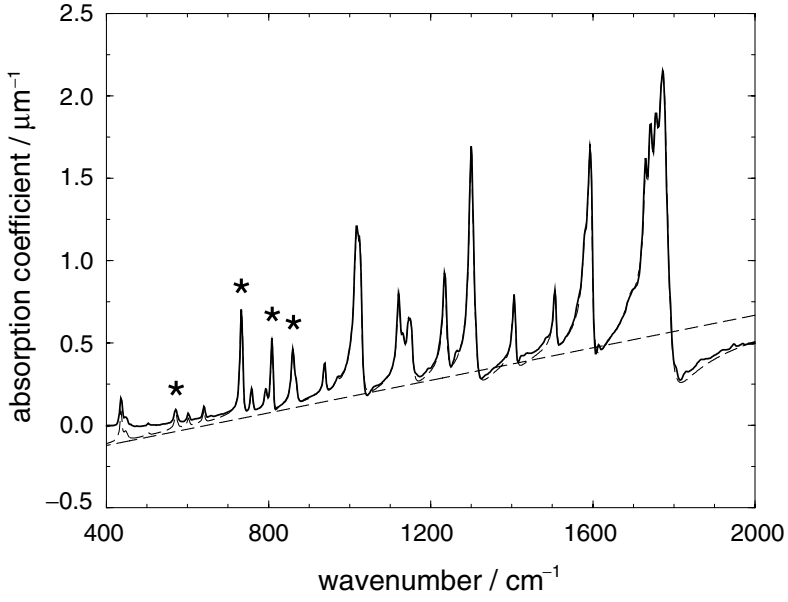

Figure 4. Absorption coefficient of the sample deposited by LA on an H-passivated Si substrate. Thick solid curve: experimental spectra; dashed curves: superimposed fit and linear background contribution (see table 1 and the explanations in section 4). Below 700 cm^{-1}, the peak areas are fitted with a more complicated background dependence than the straight line used for the calculated curve displayed in the figure. Out-of-plane modes are marked with $*$.

in-plane features, the spectra measured in p-polarized light reveal the out-of-plane features since, for increasing angle of incidence, the electric field acquires a component along the surface normal. The out-of-plane modes (marked by $*$) become more prominent for increasing angle of incidence before changing sign at the magic angle. The broad structure around 1100 cm^{-1} in the spectra at 75° is related to oxygen impurities in the substrate [22].

4. Modelling of experimental data

4.1. Dielectric function

The IR spectra of the PTCDA samples are determined by the IR-active polar modes of the molecules. Assuming an idealized film geometry with all molecules oriented in the same way (defining x as the long axis of the planar molecule, y as the short axis), the diagonal components of the dielectric tensor would be

$$\epsilon_{\alpha\alpha}(\omega) = \epsilon^{\mathrm{b}}_{\alpha\alpha} + \sum_j \frac{1}{\epsilon_0}\frac{N}{V}\left(\frac{\partial \mu^{(j)}_\alpha}{\partial Q_j}\right)^2 \frac{1}{\omega_j^2 - \omega^2 - 2\mathrm{i}\omega\gamma_j}$$
$$= \epsilon^{\mathrm{b}}_{\alpha\alpha} + \sum_j f^{(j)}_\alpha \frac{\omega_j^2}{\omega_j^2 - \omega^2 - 2\mathrm{i}\omega\gamma_j}, \qquad (1)$$

where $\epsilon^{\mathrm{b}}_{\alpha\alpha}$ are the anisotropic components of the background dielectric function, N/V the density of PTCDA molecules, ϵ_0 the vacuum permittivity, $\mu^{(j)}_\alpha$ the projection of the dipole moment of vibrational mode j on the α-axis, Q_j the normal coordinate of this mode, and

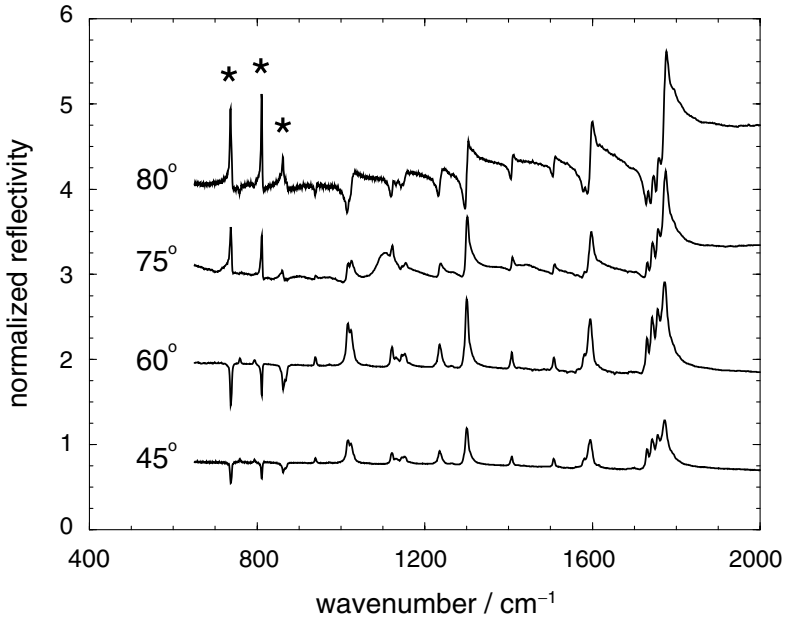

Figure 5. Reflectivity of a 220 ± 10 nm thick PTCDA film grown by OMBD on an H-passivated Si(111) substrate, normalized by the substrate reflectivity. The spectra are measured in p-polarized light for different angles of incidence, and the curves for 60°, 75° and 80° are shifted for clarity. The film is the same as the one used in figure 2. Out-of-plane modes are marked with ∗.

ω_j and γ_j the mode frequency and damping respectively. As an abbreviation, the coupling strength of each mode will be annotated as $f_\alpha^{(j)}$, corresponding to its contribution to one of the diagonal elements of the static dielectric tensor, $\epsilon_{\alpha\alpha}(0)$.

For a PTCDA film deposited on an inorganic substrate, the monoclinic crystal unit cell contains two molecules with different orientations, with both molecular planes remaining close to parallel to the substrate surface (see figure 1). The most general expression for the dielectric constant along a Cartesian direction has to account for the average orientation of the molecular axes with respect to the direction chosen:

$$\epsilon(\omega) = \sum_\alpha \langle \cos^2 \beta_\alpha \rangle \epsilon^{\mathrm{b}}_{\alpha\alpha} + \sum_j \frac{g^{(j)}\omega_j^2}{\omega_j^2 - \omega^2 - 2\mathrm{i}\omega\gamma_j}, \tag{2}$$

where β_α are the angles between the reference direction and the α-axis of a PTCDA molecules, and the brackets denote an averaging over all molecules. Therefore, the coupling strength $g^{(j)}$ of each mode contains again the expectation values of the projection cosines:

$$g^{(j)} = \sum_\alpha \langle \cos^2 \beta_\alpha \rangle f_\alpha^{(j)}. \tag{3}$$

For molecules parallel to the surface, but with random azimuthal orientation in the plane, the dielectric function in the substrate surface plane would contain the averages $\langle \cos^2 \beta_x \rangle = \langle \cos^2 \beta_y \rangle = 1/2$ and $\langle \cos^2 \beta_z \rangle = 0$. For more reactive (111)-oriented substrates like Ag(111), the monoclinic unit cells in the first monolayer of PTCDA can still grow in a well-defined geometry with respect to the substrate, allowing for six equivalent domains. After averaging over these domain orientations, the projection of the coupling strength of the in-plane IR-active molecular vibrations would again be 1/2, so that IR spectroscopy

cannot distinguish if the passivated Si(111) substrate enforces specific monolayer geometries or not.

In the monoclinic bulk phases of PTCDA, all molecules are tilted by a small angle δ, so that the projections are approximately

$$\begin{aligned} \langle \cos^2 \beta_x \rangle &= \langle \cos^2 \beta_y \rangle = \frac{\cos^2 \delta}{2} \\ \langle \cos^2 \beta_z \rangle &= \sin^2 \delta \end{aligned} \tag{4}$$

resulting in

$$g^{(j)} = (f_x^{(j)} + f_y^{(j)}) \frac{\cos^2 \delta}{2} + f_z^{(j)} \sin^2 \delta. \tag{5}$$

As the tilting angle δ is known to be small in crystalline PTCDA films (about 11° in the α-phase [23]), the cosine of δ is close to one. For powder spectra with randomly oriented crystallites, the anisotropy of the molecules is completely averaged out, so that the infrared signals are determined by the trace of equation (1):

$$\epsilon(\omega) = \tfrac{1}{3} \sum_{\alpha} \epsilon_{\alpha\alpha}(\omega), \tag{6}$$

resulting in coupling strengths $g^{(j)}$ of the IR-active modes with the same weight for all symmetry axes of the molecules:

$$g^{(j)} = \tfrac{1}{3}(f_x^{(j)} + f_y^{(j)} + f_z^{(j)}). \tag{7}$$

4.2. Choice of the background dielectric constant

For PTCDA the HOMO–LUMO transition with its transition dipole along the long axis of the molecule dominates the entire spectrum in the visible, but some higher-lying transitions contribute significantly to the static dielectric function [24]. However, already for α-PTCDA crystals with their two differently oriented molecules in the unit cell, the anisotropy between the two molecular axes in the plane is nearly averaged out by the different orientations, so that only the third diagonal component of the dielectric tensor remains much lower. In PTCDA thin films, the anisotropy of the dielectric constant was found to be quite pronounced: 4.5 for the diagonal components in the substrate plane and 1.9 for the orthogonal component [8, 25]. For our OMBD films grown on passivated Si, we have shown previously with ellipsometry that the anisotropy of the static dielectric tensor is somewhat smaller, i.e. 4.4 for the large and 2.4 for the small diagonal components [20].

Concerning the interpretation of our spectra, the background is always dominated by the two large diagonal components, with the smaller one contributing only a third or less. In order to keep the discussion simple, we take an approximate value of $\epsilon^{\mathrm{b}} = 4$ in all cases, but our statements about the average molecular orientations derived in section 5 do not depend on this choice. However, the absolute numbers for the coupling strengths of the infrared active modes in the OMBD film are affected by up to 10%, corresponding to the error margins of our numerical fitting procedure.

4.3. Absorption of the OMBD film

For an interpretation of the experimental data in figure 2, we assume a dielectric function as in equation (2), and all mode frequencies ω_j, broadenings γ_j and coupling strengths $g^{(j)}$ are left as free parameters. The multiple interferences are included with a transfer matrix scheme adapted from [26], and the fast interferences due to the thick (1 mm) substrate are integrated

out. In both the experimental and the calculated spectra a small frequency dependence of the background is taken into account by a cubic spline. The results of the numerical fit of mode frequencies and coupling strength $g^{(j)}$ are given in table 1 and figure 2. The reliability of the fit is better than 10% for coupling strengths of isolated modes above 700 cm^{-1}, while for groups of modes with small splittings, only the sum of the coupling strengths is defined within this error margin whereas the individual uncertainties of the sub-peaks are larger by about a factor of 2. Below 700 cm^{-1}, the peak areas had to be fitted with a strongly frequency-dependent background, which leads to a fitting error of the order of a third. Furthermore, for the OMBD film, the PTCDA modes were obscured by two-phonon lines of the substrate at 605 and 618 cm^{-1} (TO + TA phonon [22, 27, 28]), and the molecular out-of-plane mode near 570 cm^{-1} could not be fitted due to a broad structure in this frequency region, probably related to a LO + TA two-phonon line of Si [22, 27, 28].

4.4. Powder spectra

The asymmetric peaks in figure 3 are simulated by scattering contributions to the powder reflectivity. More specifically, we fit the spectra with the following formula:

$$R(\omega) = R_0(\omega) + R_1(\omega) + R_2(\omega), \tag{8}$$

where R_0 is a smooth (polynomial) background function, and R_1 and R_2 are contributions depending mainly on the real and imaginary parts of the refractive index $n(\omega) = [\epsilon(\omega)]^{1/2}$, respectively. For R_2, we assume a dependence as in the extinction coefficient due to scattering at absorbing particles [29]

$$R_2(\omega) = -c_2 \operatorname{Im}\left(\frac{\epsilon(\omega) - 1}{\epsilon(\omega) + 2}\right), \tag{9}$$

where Im denotes the imaginary part. For R_1, we found empirically that a formula combining the *large* sphere limit for the frequency dependence of the extinction coefficient due to Mie scattering [30] with the dependence on the refractive index as the leading order of Mie scattering for *small* spheres [29] leads to a good fit of the reflectivity:

$$R_1(\omega) = -c_1\omega^2 \operatorname{Re}\left[\left(\frac{\epsilon(\omega) - 1}{\epsilon(\omega) + 2}\right)^2\right] \tag{10}$$

where Re denotes the real part. The above formulae for powder reflectivity, equations (8)–(10), include a non-trivial frequency-dependent ratio of contributions depending mainly on the imaginary and real parts of the refractive index. Using these equations, and a dielectric function where the resonance frequencies ω_j, dampings γ_j and coupling strengths $g^{(j)}$ are left again as free parameters, we obtain an excellent fit of the measured signals (compare figure 3).

For the powder reflectivity, no absolute sample thickness can be derived, so that the overall scaling of the corresponding entries in table 1 is arbitrary. However, with the scaling chosen, and the above dependence on frequency and refractive index as in equations (8)–(10), all entries in table 1 for *in-plane* modes are similar to the coupling strengths for the OMBD film, indicating that the assumed dependence on frequency and refractive index is realistic. Our data analysis demonstrates that powder reflectivity can be used as a quantitative reference, avoiding therefore any contamination of the vibrational spectra of the molecules with a matrix material, e.g. the commonly used KBr pellet.

4.5. Absorption of the film deposited with laser ablation

For the sample produced by LA we have searched again for a smooth interpolation formula accounting approximately for the frequency dependence of the absorptive and dispersive

Table 1. Frequencies (in cm^{-1}) and coupling strengths of the IR-active modes of PTCDA fitted to the experimental IR signals. In the frequency range investigated, 22 out of the total of 46 IR-active molecular vibrations contribute significantly (see table 2 for assignments). First two columns: modes fitted to the transmission of a 220 ± 10 nm thick PTCDA film grown by OMBD on an H-passivated Si(111) substrate (compare figure 2 and equations (2) and (3)). The features at 605 and 618 cm^{-1} are substrate modes. Next two columns: mode frequencies and coupling strengths fitted to the powder reflectivity spectra of randomly oriented PTCDA crystallites deposited on a gold mirror (compare figure 3 and equations (8)–(10)). For the powder spectrum, the overall scaling is chosen in order to have coupling strengths of the in-plane modes similar to the OMBD film. The last two columns contain the mode frequencies and coupling strengths obtained for the 1.3 μm thick film grown with LA (see figure 4). Out-of-plane vibrations are denoted by $*$. Their quite different coupling strengths in the different samples reveal differences in the preferential orientation of the molecules. In all cases, a background dielectric constant of 4 was assumed.

OMBD film absorption		Powder reflectivity		LA film absorption	
ω_j (cm^{-1})	$g^{(j)}$ ($\times 10^{-3}$)	ω_j (cm^{-1})	$g^{(j)}$ ($\times 10^{-3}$)	ω_j (cm^{-1})	$g^{(j)}$ ($\times 10^{-3}$)
436	13	436	8	437	18
449	6	454	7	448	10
503	1	512	2	504	1
		570*	16	572*	7
602	3	602	2	603	3
605	9				
618	2				
641	3	641	3	641	3
733*	2.7	728*	76	732*	16
				735*	12
759	4	759	4	759	5
794	2	794	4	794	3
809*	0.8	807*	31	807*	7
				810*	5
860*	1.3	859*	25	860*	9
869*	0.5	868*	7	867*	5
939	4	939	4	939	4
972	1	972	1	971	1
1017	33	1015	61	1018	39
1024	20	1027	12	1026	14
1121	11	1122	14	1121	8
1133	6	1132	3	1132	7
		1138	2		
1145	3	1145	4	1145	4
1152	7	1152	13	1152	9
1236	14	1235	18	1235	12
1300	38	1300	38	1300	22
				1307	10
1407	5	1407	6	1406	6
1508	4	1508	5	1508	4
1580	5	1579	5	1581	5
1594	26	1593	22	1594	17
		1599	5		
1696	2			1696	2
1731	7	1730	20	1731	3
1743	19	1743	3	1743	9
1756	17	1755	16	1756	7
1770	49	1773	51	1774	43

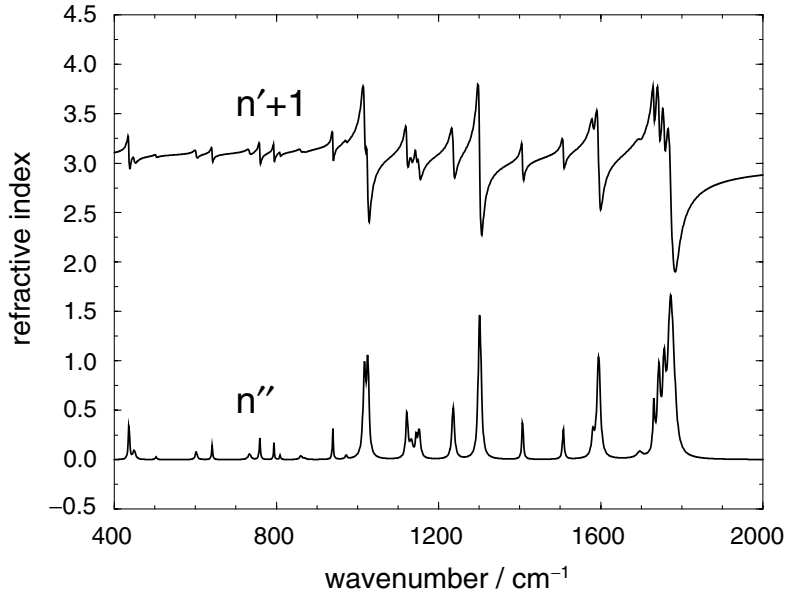

Figure 6. Refractive index as calculated from the dielectric function fitted to the absorption spectra of the OMBD film in figure 2. Lower: imaginary part $n'' = \mathrm{Im}[n]$ of refractive index, upper: real part $n' = \mathrm{Re}[n]$, shifted by +1 for clarity. The modes at 605 and 618 cm^{-1} related to the Si substrate are not included in the calculated refractive index.

contributions to the experimental data. We found empirically that the absorption coefficient derived from the logarithm of the transmission can be modelled as

$$\alpha(\omega) + c_1\omega^2(\mathrm{Re}[n(\omega)] - n^{\mathrm{b}}) + c_2\omega, \tag{11}$$

where $n^{\mathrm{b}} = [\epsilon^{\mathrm{b}}]^{1/2}$ is the refractive index derived from the background dielectric constant, and the leading term α is given as usual by the imaginary part of the refractive index, $\alpha(\omega) = 2\,\mathrm{Im}[n(\omega)]\omega/c$. The second and third term in (11) account for the decrease of the IR transmission at higher frequencies due to scattering at the rough surface of the PTCDA film.

Due to this rough sample surface, the average film thickness of the laser-ablated sample cannot be measured by optical methods, so that it has to be derived from a comparison with the absorption coefficient of the OMBD-grown film. For the absolute scaling of the IR coupling strengths of the laser-ablated sample, we use the modes between 1000 and 1200 cm^{-1} in table 1, determining also the *effective* film thickness of 1.1 μm for the in-plane modes. However, for higher frequencies, the relative coupling strengths of the laser-ablated sample diminish by about two-thirds, indicating that the assumed frequency dependence still has some weaknesses.

4.6. Comparison of absorption and reflectivity of OMBD films

From the dielectric function fitted to the absorption spectra of the OMBD film in figure 2, we can derive the refractive index (compare figure 6 for the real and imaginary parts). At small angles of incidence, the features in the reflectivity spectra correspond quite well to the imaginary part of the calculated refractive index, while at increasing angles of incidence, the real part of the refractive index gains importance. However, the completely different behaviour of the out-of-plane modes at large angles of incidence as in figure 5 is not accounted for because

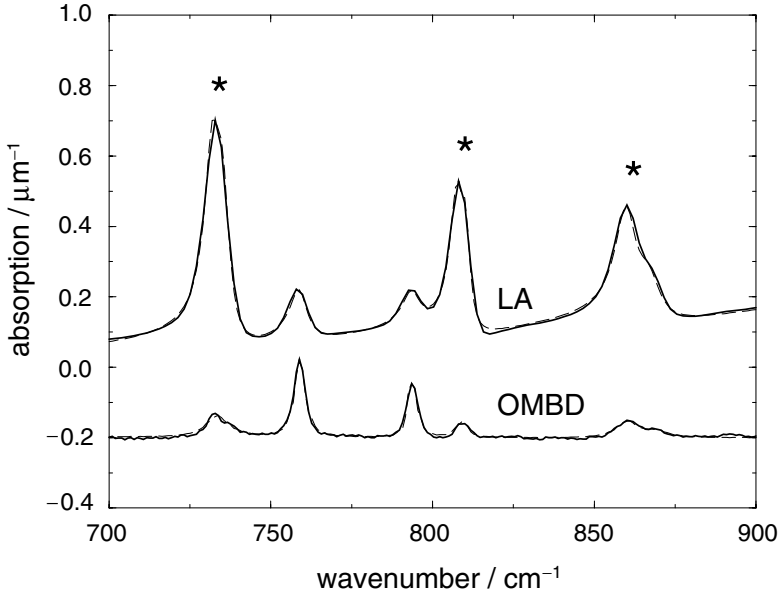

Figure 7. Comparison of the absorption of the OMBD and LA samples in the region of the out-of-plane modes. For the in-plane modes, the larger broadenings in the LA sample indicate a more random influence of neighbouring molecules on each other. Thick solid curves: experimental spectra, dashed curves: superimposed fit (see table 1 and the explanations in section 4). The spectra of the OMBD film are shifted by −0.2 for clarity.

the dielectric function used in the calculation was derived from the absorption spectra at normal incidence where the contribution of the molecular out-of-plane modes is small.

5. Average orientation of PTCDA molecules

Comparing the OMBD film transmission and powder reflectivity spectra, it is found that the *in-plane* molecular vibrations occur with similar coupling strengths over the whole frequency range, demonstrating that the assumed frequency dependence for the powder spectrum accounts for the dominating features. However, for the *out-of-plane* modes at 733(728) cm^{-1}, 809(807) cm^{-1} and for the split mode at 860(859) and 869(868) cm^{-1} in the film (powder) spectra, the coupling strengths differ significantly. For an estimate of the average orientation of the molecules in the different samples, we calculate the ratio of the sum of coupling strengths of the out-of-plane modes between 700 and 900 cm^{-1} and the corresponding sum of the in-plane modes between 1000 and 1200 cm^{-1} for each of the three samples, giving $5.3/80 = 0.066$ for the OMBD film, $139/109 = 1.275$ for the powder reflectivity and $54/81 = 0.667$ for the LA sample. The pronounced differences of the out-of-plane modes in the OMBD and LA-deposited films are reported in figure 7, revealing also the similar peak areas for the in-plane modes, but with somewhat larger peak widths in the LA-deposited film due to the lower degree of crystalline order.

As the crystallites in the powder can be assumed to have a random orientation, this sample yields directly the ratio of the contributions to the dielectric function (compare equation (7)). Using this reference value, equation (5) for the OMBD film can be used to estimate the average tilting angle:

$$\frac{2\sin^2\delta}{\cos^2\delta} = \frac{0.066}{1.275} = 0.052, \tag{12}$$

yielding $\delta \approx 9°$, comparing favourably with the tilting angle in α-PTCDA known from x-ray scattering, $\delta \approx 11°$ [23]. The low average tilting angle derived from our IR spectra of the OMBD film and the reasonable agreement with previous investigations indicate the good crystallinity of our sample. For the LA film, we find

$$\frac{\langle\cos^2\beta_z\rangle}{\langle\cos^2\beta_x\rangle} = \frac{\langle\cos^2\beta_z\rangle}{\langle\cos^2\beta_y\rangle} = \frac{0.667}{1.275} = 0.52 \approx \frac{1}{2}, \tag{13}$$

giving roughly

$$\begin{aligned} &\langle\cos^2\beta_x\rangle = \langle\cos^2\beta_y\rangle \approx 0.4, \\ &\langle\cos^2\beta_z\rangle \approx 0.2. \end{aligned} \tag{14}$$

This demonstrates that the presence of a planar substrate still influences the preferential orientation of the PTCDA molecules. The effective LA film thickness of 1.1 μm estimated from the relative strengths of the in-plane modes with respect to the 220 nm OMBD sample has to be corrected for the different averages of the projection cosines, yielding a somewhat larger LA film thickness of about 1.3 μm. The larger average deviation between molecule normal and substrate normal in the LA film indicates that the growth dynamics of the PTCDA crystallites becomes more important than for the OMBD film, whereas the remaining part of the preferential orientation can still be related to the favourable flat adsorption geometry of the molecules in the first monolayer.

6. Mode assignment

6.1. Single molecule

The mode frequencies observed in the films grown by OMBD agree quite well with earlier IR spectra for PTCDA in KBr pellets [10] (see the first two columns in table 2).

As was shown recently for the Raman-active A_g modes of PTCDA [31], reliable vibrational frequencies can be obtained with a tight-binding approach to density functional theory [32], called DFTB in the following. Applying the same method, we assign the observed features of the infrared spectra discussed in the present work to the calculated polar mode frequencies of an isolated PTCDA molecule. The resulting mode frequencies are presented in table 2 together with the contributions of C, H and O to the vibrational eigenvectors. The agreement between calculated and measured vibrational modes allows a one-to-one assignment for the most prominent experimental features. Furthermore, most of the calculated eigenvectors agree quantitatively with calculations based on the B3LYP method [33] and larger variational basis sets [34]. In a recent comparison of DFTB and B3LYP calculations with HREELS spectra of PTCDA, it was found that the DFTB method gives somewhat larger deviations from the experimental positions of the IR-active modes than methods with larger variational basis [35]. In most cases, the DFTB assignments in table 2 coincide with previous suggestions [10], with some changes concerning especially the region of the δ_{CH} modes and the asymmetric anhydride mode occurring at 1052 cm^{-1} in the DFTB calculation, corresponding to the observed split mode around 1020 cm^{-1}.

6.2. Experimental mode splittings

As the four carboxylic dipoles on the corners of PTCDA lead to a quadrupole moment of the whole molecule, the neighbouring molecules in the monoclinic crystal adjust nearly coplanar, but with the long axes approximately orthogonal to each other. For strongly absorbing IR-active modes localized on the periphery of the molecule, the dipole–dipole interaction between

Table 2. Comparison of experimental IR mode frequencies of PTCDA according to [10] (first column), the mode frequencies observed in the epitaxial OMBD film deposited on H-passivated Si(111) (second column), with the modes at (504), (572) and (603) taken from the LA-deposited film where the substrate lines are less disturbing. Third column: vibrational frequencies of a single molecule calculated with the DFTB method. The next three columns give the contributions of carbon, hydrogen and oxygen to the squared vibrational eigenvectors, and the last two columns contain the symmetry character (x, long axis; y, short axis of the molecule; z, out-of-plane) and an assignment of the elongation pattern, where ν stands for stretch and δ for bend. The most prominent part of the elongation pattern is always given first. For pairs of split modes, the calculated mode frequency is reported in the line of the lower experimental frequency. Using averages of the observed split mode pairs for a comparison between experimental and calculated mode frequencies, the rms deviation is 34 cm^{-1}. The assignment of the internal modes was guided by the calculated IR coupling strengths and the correspondence between the vibrational eigenvectors obtained with different theoretical approaches [34].

Reference [10] KBr pellet	OMBD film (LA film)	DFTB calc.	C (%)	H (%)	O (%)		Interpretation
438	436	427	70	5	26	y	$\delta_{C–C–O}$, $\delta_{C–C=O}$
503	(504)	507	54	4	41	x	$\delta_{C–C–O}$, $\nu_{C–O}$
572	(572)	531	94	0	6	z	δ_{CC}, long axis folding
603	(603)	625	83	4	13	y	δ_{CCC}, $\delta_{C–C=O}$
641	641	652	62	4	34	x	$\delta_{C–O–C}$, $\delta_{C–C–O}$, δ_{CCC}
734	733	695	89	3	8	z	δ_{CCC}, $\delta_{O=C–O}$, $\delta_{C–O–C}$
759	759	720	75	10	15	x	δ_{CCC}, $\delta_{C–C–O}$
809	809	769	95	4	1	z	δ_{CCC}, δ_{CH}
862	860	818	27	73	0	z	δ_{CH}
	869						
938	939	983	81	6	13	x	δ_{CC}, $\nu_{C–O}$, δ_{CH}
	1017	1052	55	4	40	y	$\nu_{C–O}$, ν_{CC}, δ_{CH}
1025	1024						
1122	1121	1147	60	32	8	x	δ_{CH}, $\nu_{C–O}$
	1133						
	1145	1164	41	57	1	y	δ_{CH}
1150	1152						
		1189	68	31	1	y	δ_{CH}
1234	1236	1259	81	17	2	y	δ_{CH}, ν_{CC}
1300	1300	1304	55	42	3	x	δ_{CH}
1406	1407	1364	82	18	0	y	δ_{CH}, ν_{CC}
1506	1508	1476	85	13	1	x	ν_{CC}, δ_{CH}
	1580	1623	91	8	1	x	ν_{CC}, δ_{CH}
1594	1594	1646	95	5	0	x	ν_{CC}, δ_{CH}
1731	1731	1690	61	0	39	y	$\nu_{C=O}$
1744	1743						
1756	1756	1717	65	0	35	x	$\nu_{C=O}$
1772	1770						

the vibrational modes of the two molecules in the unit cell leads to a pronounced splitting. This is best seen for the highest out-of-plane modes measured at 860 and 869 cm^{-1} in the OMBD film, the antisymmetric anhydride stretching modes at 1017 and 1024 cm^{-1}, the four δ_{CH} modes measured between 1121 and 1152 corresponding to only two modes of the isolated molecule, and the four $\nu_{C=O}$ carboxylic stretching modes above 1700 cm^{-1}, corresponding again to only two molecular vibrations. As expected for the dipole–dipole interaction, the carboxylic stretching modes with the strongest absorption show the largest splitting. The resulting four modes depend sensitively on small geometric changes, as can be seen from the

Table 3. Calculated Davydov splittings of the Γ point phonons arising from strongly IR-active internal molecular vibrations. The contributions of the different types of atoms to the eigenvector are given in %, and the orientation of the dipole moment is given in terms of the unit vectors for the α and the β phase shown in figure 1. For the b vector corresponding to the C_2 axis of the monoclinic group this projection is exact, whereas for phonons with a different orientation of the dipole moment, the given projection is approximate.

α-PTCDA (cm^{-1})	C (%)	H (%)	O (%)		β-PTCDA (cm^{-1})	C (%)	H (%)	O (%)	
1031	64	6	30	b	1036	62	5	33	c'
1040	63	7	29	c'	1044	62	6	31	b
1667	63	0	37	b	1668	63	0	37	c'
1680	64	0	36	c'	1682	64	0	36	b
1705	66	0	34	c'	1700	67	0	33	b
1711	66	0	34	b	1706	66	0	33	c'

results in table 1: for the three samples studied, pronounced changes for the relative intensities occur, while the frequency positions are similar, except for the highest mode which shows a relatively large variation of four wavenumbers. The large changes of the relative intensities, especially for the two lower C=O stretching modes at 1731 and 1743 cm^{-1}, indicate different coupling strengths in the α phase (samples grown by OMBD and LA) and in the β phase (powder spectra) of PTCDA.

6.3. Calculated mode splittings

The vibrational modes of the α and β phase have been calculated with the DFTB approach for the corresponding optimized atomic geometries. In both cases, the Brillouin zone was sampled with four wavevectors which can be reduced to two irreducible $\boldsymbol{k}$-points. This sampling corresponds to the smallest set of wavevectors with roughly equidistant wavevectors in all three directions of the Brillouin zone. As the energy functional used does not include any van der Waals interaction, the variation of the stacking vector does not produce an energetic minimum in the experimental crystal geometry. Therefore, the calculations were performed for fixed lattice vectors, and all atomic positions in the unit cell were optimized with a conjugate gradient scheme. For the α phase, the rms deviation of the atomic positions from the geometry determined by electron diffraction [36] is 0.6% of the short (b) and long (c') lattice vectors displayed in figure 1. For the β phase, this deviation is 0.7% of the long (b) and 1.4% of the short (c') lattice vector. Furthermore, the tilting angle of the molecules with respect to the planes displayed in figure 1 is slightly changed, mainly due to the lack of van der Waals corrections.

The calculated frequencies of the three vibrational modes with the largest measured Davydov splittings are shown in table 3. For the ν_{C-O} modes near 1000 cm^{-1}, the changes in the contributions to the eigenvectors with respect to the calculated mode in table 2 reveal a mixing with different internal vibrations of the isolated molecule, especially the mode at 983 cm^{-1} in table 2. This does not contradict the selection rules in the monoclinic space group: as the point group for each of the molecules is reduced to $C_i = \{E, I\}$, all molecular modes of the same parity belong to the same representation.

In the region of the $\nu_{C=O}$ modes, the splitting of the lower pair is reproduced reasonably well, whereas the splitting of the upper mode pair is severely underestimated. From reference calculations with the B3LYP method and different variational basis sizes [34], we found a strong dependence of the dipole coupling strength on the corresponding molecular mode.

For too small a basis size, the polarizability of the non-bonding oxygen orbitals is strongly underestimated, resulting therefore in too low a dipole moment. A similar shortcoming occurs in the minimal valence basis used in the DFTB approach, so that the too small dipole moment of this molecular mode results in an underestimate of the Davydov splitting in both crystal phases.

From the projection of the dipole moments on the lattice unit vectors it is obvious that the arrangement of the two nearly coplanar molecules in the plane determines the splitting and the ordering of the mode frequencies with respect to the long and short axis of the rectangular unit cell displayed in figure 1. Even though the DFTB calculations allow us to assign the most prominent features in the IR spectra to molecular modes, the calculated Davydov splittings are not precise enough for an unambiguous assignment of the two different monoclinic phases to the measured IR spectra. However, some of the calculated results like the orientation of the dipole moments with respect to the crystal unit vectors in table 3 could easily be checked for single crystals.

7. Summary

In the present work, PTCDA films grown on H-passivated Si by OMBD and by LA have been studied using infrared spectroscopy. On the macroscopic scale of our infrared spot size of 1 mm, we find isotropy within the substrate plane, indicating a random orientation of the long and short axis of the molecules within this plane, and consequently a random orientation of the monoclinic crystallites. However, for the OMBD-grown sample, all molecules are lying nearly flat on the substrate, with a small tilting angle of the order of 9°. The reasonable agreement with the value of 11° observed on α-PTCDA crystals with x-ray scattering underlines the good crystallinity of the films. Owing to this preferential orientation, a strong anisotropy between the substrate plane and its normal could be observed. Assuming that the β-PTCDA powder contains randomly oriented crystallites, it could be demonstrated that in the laser-ablated films, the orientation of the PTCDA molecules was not yet completely randomized, but a flat-lying geometry of the molecules in the film was still slightly favoured. From the first density functional calculation of the vibrational modes for both monoclinic bulk phases, we have obtained a projection of the dipole moments on the crystal lattice vectors, and for modes weakly affected by the atomic polarizabilities, the calculated Davydov splittings were in good agreement with the experimental findings.

Acknowledgments

The authors thank N Vogel and N Kochan for the preparation of PTCDA films by LA, and S Schlemmer for clarifying discussions concerning light scattering. Financial support by the Human Potential Research Training Network DIODE (contract no HPRTN-CT-1999-00164) and by the Deutsche Forschungsgemeinschaft is gratefully acknowledged.

References

[1] Forrest S R 1997 *Chem. Rev.* **97** 1793
[2] Nelson S F, Gundlach D J and Jackson T N 1998 *Appl. Phys. Lett.* **72** 1854
[3] Tung W and van Slyke S A 1987 *Appl. Phys. Lett.* **51** 913
[4] Burrows P E and Forrest S R 1993 *Appl. Phys. Lett.* **62** 3102
[5] Taylor R T, Burrows P E and Forrest S R 1997 *IEEE Photon. Technol. Lett.* **9** 365

[6] Kendrick C and Kahn A 1998 *Appl. Surf. Sci.* **123/124** 405
[7] Umbach E, Sokolowski M and Fink R 1996 *Appl. Phys.* A **63** 565
[8] Fuchigami H, Tanimura S, Uehara Y, Kurata T and Tsunoda S 1995 *Japan. J. Appl. Phys.* **34** 3852
[9] Antunes P A, Constantino C J L and Aroca R 2001 *Appl. Spectrosc.* **55** 1341
[10] Akers K, Aroca R, Hor A and Loutfy R O 1987 *J. Phys. Chem.* **91** 2954
[11] Böhringer M, Schneider W-D, Glöckler K, Umbach E and Berndt R 1998 *Surf. Sci.* **419** L95
[12] Chizhov I, Kahn A and Scoles G 2000 *J. Cryst. Growth* **208** 449
[13] Murakami M, Iijima S and Yoshimura S 1986 *J. Appl. Phys.* **60** 3856
[14] Kamo H, Yudakasa M, Kurita S, Matsui T, Kikushi R, Ohki Y and Yoshimura S 1994 *Synth. Met.* **68** 61
[15] Uder B, Ludwig C, Petersen J, Grompf B and Eisenmenger W 1995 *Z. Phys.* B **97** 389
[16] Morozov A O, Kampen T U and Zahn D R T 2000 *Surf. Sci.* **446** 193
[17] Kampen T U, Tenne D A, Park S, Salvan G, Scholz R and Zahn D R T 1999 *Phys. Status Solidi* b **215** 431
[18] Yudasaka M, Tasaka Y, Tanaka M, Kamo H, Ohki Y, Usami S and Yoshimura S 1994 *Appl. Phys. Lett.* **64** 3237
[19] Nishio S, Mase R, Oba T, Matsuzaki A and Sato H 1998 *Appl. Surf. Sci.* **127–129** 589
[20] Friedrich M, Wagner T, Salvan G, Park S, Kampen T U and Zahn D R T 2002 *Appl. Phys.* A **75** 501
[21] Kaiser R, Friedrich M, Schmitz-Hübsch T, Sellam F, Hohenecker S, Kampen T U, Leo K and Zahn D R T 1999 *Fresenius J. Anal. Chem.* **363** 189
[22] Mead D G and Lowry S R 1980 *Appl. Spectrosc.* **34** 167
[23] Lovinger A J, Forrest S R, Kaplan M L, Schmidt P H and Venkatesan T 1984 *J. Appl. Phys.* **55** 476
[24] Vragović I, Scholz R and Schreiber M 2002 *Europhys. Lett.* **57** 288
[25] Zang D Y, So F F and Forrest S R 1991 *Appl. Phys. Lett.* **59** 823
[26] Harbecke B, Heinz B, Offermann V and Theiß W 1996 Far-infrared spectroscopy *Optical Characterization of Epitaxial Semiconductor Layers* ed G Bauer and W Richter (Berlin: Springer) p 203
[27] Collins R J and Fan H Y 1954 *Phys. Rev.* **93** 674
[28] Johnson F A 1959 *Proc. Phys. Soc.* **73** 265
[29] van de Hulst H C 1981 *Light Scattering by Small Particles* (New York: Dover) ch 14.22
[30] van de Hulst H C 1981 *Light Scattering by Small Particles* (New York: Dover) ch 11.22
[31] Scholz R, Kobitski A Yu, Kampen T U, Schreiber M, Zahn D R T, Jungnickel G, Elstner M, Sternberg M and Frauenheim T 2000 *Phys. Rev.* B **61** 13659
[32] Elstner M, Porezag D, Jungnickel G, Elsner J, Haugk M, Frauenheim T, Suhai S and Seifert G 1998 *Phys. Rev.* B **58** 7260
[33] Becke A D 1988 *Phys. Rev.* A **38** 3098
Lee C, Yang W and Parr R G 1988 *Phys. Rev.* A **37** 785
[34] Kobitiski A Yu, Scholz R and Zahn D R T 2003 *J. Mol. Struct.: THEOCHEM* **625** 39
[35] Tautz F S, Sloboshanin S, Schaefer J A, Scholz R, Shklover V, Sokolowski M and Umbach E 2000 *Phys. Rev.* B **61** 16933
[36] Ogawa T, Kuwamoto K, Isoda S, Kobayashi T and Karl N 1999 *Acta Crystallogr.* B **55** 123